

Theoretical Analysis of a 2D Metallic/Semiconducting Transition-Metal Dichalcogenide NbS₂//WSe₂ Hybrid Interface

Zahra Golsanamlou, Luca Sementa, Teresa Cusati, Giuseppe Iannaccone, and Alessandro Fortunelli*

A first-principles theoretical study of a monolayer-thick lateral heterostructure (LH) joining two different transition metal dichalcogenides, NbS₂ and WSe₂, is reported. The NbS₂//WSe₂ LH can be considered a prototypical example of a metal (NbS₂)/semiconductor (WSe₂) 2D hybrid heterojunction. First, realistic atomistic models of the NbS₂//WSe₂ LH are generated and validated, its band structure is derived, and it is subjected to a fragment decomposition and electrostatic potential analysis to extract a simple but quantitative model of this interfacial system. Stoichiometric fluctuations models are also investigated and found not to alter the qualitative picture. Then, electron transport simulations are conducted and they are analyzed via band alignment analysis. It is concluded that the NbS₂//WSe₂ LH appears as a robust seamless in-plane 2D modular junction for potential use in optoelectronic devices going beyond the present miniaturization technology.

The number of studies in 2DMs based on TMDC has increased exponentially since the first preparation of atomically thin exfoliated sheets of TMDC (such as MoS₂, NbSe₂ or WS₂), and especially after their successful synthesis via chemical vapor deposition (CVD).^[3] Although the detailed growth mechanism is still matter of debate^[4–6], soon afterward the first successful preparation of pure phases, the CVD synthesis protocols were extended to composite materials, enabling the synthesis of both vertical (VH) and lateral (LH) heterostructures joining two different TMDCs, and the exploration of their transport and optoelectronics features.^[7–10] Different combinations of LHs and VHs of 2D-TMDCs have therefore been prepared and subject to extensive research.


LHs, in particular, offer the possibility of investigating and exploiting seamless and atomically sharp in-plane heterostructures, realizing the ultimate thickness limit for conducting/semiconducting junctions, in principle suitable to build an integrated circuit technology that could be competitive, at the fundamental level of control of the electrostatic potential in the device, with present silicon-based technology.^[11,12] At the nanometer scale, first-principles quantum-mechanical (QM) simulations with atomistic detail are needed to predictively model fundamental interactions and the basic behavior of single material and interfaces. The first step of a proper multiscale approach must therefore start from QM modeling and simulations.^[13–15] Indeed, multiscale simulations have shown to be able to predict transmission properties with a comparable accuracy with respect to experiment.^[16,17] Such a predictive ability can be combined with the precise knowledge of the atomistic structure of the investigated systems, and therefore the possibility of obtaining accurate information on both ideal (nondefective) and nonideal (defective) systems,^[18] so as to give information on the maximum achievable value of any given property, as well as, indirectly, information on the level of defectivity of the experimental system.^[19] More in general, accurate data on well-defined configurations as provided by computational studies lay the foundation of structure/property relationships, especially when analysis tools are developed that allow one to understand and interpret in depth both computational and experimental results.^[17]

1. Introduction

2D materials (2DMs),^[1] made up of few-atom-thick layers of transition metal dichalcogenides (TMDCs), are attracting increasing interest in both science and technology for their peculiar charge transport and optical response properties which promise to be exploitable, e.g., in future optoelectronic devices.^[2]

Dr. Z. Golsanamlou, Dr. L. Sementa, Dr. A. Fortunelli
CNR-ICCOM and IPCF
Consiglio Nazionale delle Ricerche
via G. Moruzzi 1, Pisa 56124, Italy
E-mail: alessandro.fortunelli@cnr.it

Dr. T. Cusati, Dr. G. Iannaccone
Dipartimento di Ingegneria dell'Informazione
Università di Pisa
Via G. Caruso 16, Pisa 56122, Italy

 The ORCID identification number(s) for the author(s) of this article can be found under <https://doi.org/10.1002/adts.202000164>

© 2020 The Authors. Advanced Theory and Simulations published by Wiley-VCH GmbH. This is an open access article under the terms of the Creative Commons Attribution-NonCommercial-NoDerivs License, which permits use and distribution in any medium, provided the original work is properly cited, the use is non-commercial and no modifications or adaptations are made.

The copyright line for this article was changed on 27 April 2021 after original online publication.

DOI: 10.1002/adts.202000164

Experimentally, Zhang et al. studied edge effects in MoS₂//WSe₂ monolayer (ML)/bilayer lateral heterojunctions^[20] and determined the alignment of the valence band maximum and conduction band minimum of the two semiconductors at the LH. Li et al. were able to grow devices based on WS₂//WSe₂ LHs and explored sulfurization effects,^[21] finding that the replacement of W–Se by W–S bonds at the interface increased the system stability, improved the efficiency of electron transport, and decreased the Schottky barrier. The Schottky barrier was also measured for the NbS₂//MoS₂ VH heterostructure by Shin et al.,^[22] studying in particular how the doping concentration affects Schottky barrier height and the system's transport properties.

Same-material heterostructures (i.e., two different phases of the same stoichiometrically identical material) have been studied at both experimental and theoretical levels for 2H/1T (or 1T') lateral interfaces,^[23–25] revealing a consistency between theoretical and experimental pictures, such as the numerical values of the Schottky barriers or more exotic topological-insulating phenomena.^[26] It has also been shown that the influence of the contact metal electrode should be considered in some cases to reconcile theory and experiment.^[23]

At the theoretical level, density-functional theory (DFT) has been employed to study several TMDC heterostructures, such as in-plane WS₂//WSe₂//MoS₂ LH.^[27] Some studies used nanoribbon models of TMDC LHs (e.g., MoS₂//WS₂ LH nanoribbons with 14.6 Å width and different lengths^[28]), and analyzed their electronic structure and transport properties, finding a strong dependence of transport on the configuration of the edges, whether zig-zag or armchair, in keeping with the fact that charge transport was found to mostly occur along the edges.^[28–30] Ding et al. investigated metal/metal NbS₂//black phosphorus and NbS₂//metallic(T-phase)-WSe₂ VHs,^[31] finding that the high work function of NbS₂ stabilizes p-type ohmic contact for both VHs. A comparative charge analysis suggested the importance of a sufficiently large work function in one electrode to compensate the reduction in work function due to interfacial dipoles. MoS₂//WS₂ and MoSe₂//WSe₂ VH systems were studied by Zhu et al.,^[32] who rationalized the evolution of the *k*-resolved band structure of these systems for different stacking configurations in terms of the interplay between orbital splitting and charge transfer effects. Cao et al.^[33] focused on MoS₂//WSe₂ LH and on the influence of stoichiometric randomization at the interface. A limited number of stoichiometric swappings between S and Se atoms was found to have a minor effect on the electrostatic potential profile at the junction, whereas a more extensive defectivity level was found to smoothen the electrostatic potential profile, reducing the ability of the device to promote exciton dissociation. Jelver et al. calculated Schottky barrier height of 2D metal–semiconductor junctions,^[16] considering the slope of the density of states (DOS) and estimating barrier height from values of transmission. They also studied how a higher doping level and the presence of localized interface states can modulate the barrier height.

Here we conduct a first-principles theoretical study of a NbS₂//WSe₂ LH as a prototypical example of metal/semiconductor hybrid heterostructures. After generating realistic atomistic models of the NbS₂//WSe₂ LH and of its band structure, we use fragment decomposition and electrostatic

potential analysis to arrive at a physically simple and quantitatively precise modeling of this interphase. Explicit transmission simulations confirm the expectations of our modeling, with consistency further demonstrated via a band alignment analysis of the transmission results. We conclude that the NbS₂//WSe₂ LH appears as a robust and potentially useful modular junction for use in optoelectronic devices. This is further supported by investigating stoichiometric fluctuations at the interface, corresponding to stoichiometrically nonsharp interfaces possibly produced at the experimental level, which shows that such phenomena can indeed occur but should not alter qualitatively (or even reinforce) the robustness and potential use of this system.

The article is organized as follows. The computational method and analysis protocol are presented in Section 2. Section 3 is devoted to presenting and discussing our main results: structure prediction, band alignment, transmission simulations and their analysis, stoichiometry fluctuations. Conclusions are summarized in Section 4.

2. Computational and Theoretical Method

2.1. Computational Details

Geometry optimizations and electronic structure calculations were carried out within first-principles DFT using the Quantum Espresso (QE) package.^[34,35] A plane-wave basis set, a gradient-corrected exchange-correlation functional (Perdew–Burke–Ernzerhof (PBE))^[36] augmented with terms describing dispersion interactions in the Grimme-D3 formalism,^[37] and scalar-relativistic ultrasoft pseudopotentials (US-PPs) were utilized. Pure NbS₂ and WSe₂ hexagonal phases were described for convenience using orthogonal unit cells. Monkhorst–Pack *k*-meshes of 12 × 22 × 1 and 1 × 22 × 1 were used for the unit cell and the scattering region, respectively, to sample the Brillouin zone (BZ). We used an energy cutoff of 50 Ry for the selection of the plane-wave basis set to describe the wave function and 500 Ry for the electron density, and a vacuum of 22 Å was used to minimize interactions with replicated unit cells.

Transmission simulations were performed using the PWCOND routine within QE, based on a scattering-state approach (a scattering theory for rightward propagating modes from the left to the right electrode^[38]) which integrates numerically a scattering equation in real space along the direction of transport according to the formula: $T = \sum_{mn} |T_{mn}|^2 = \text{Tr}[\mathbf{T}^+\mathbf{T}]$, where *m* (*n*) is related to all the propagating and decaying states on the left (right) leads and **T** is the matrix of normalized transmission amplitudes, $T_{mn} = \sqrt{\frac{I_m}{I_n}} t_{mn}$. Here, *I_m* and *I_n* are the currents carried by the state *m* and *n*, respectively.^[38,39] This approach applies in the limit of ballistic transport and corresponds to ideal transmission in the absence of defects. In this case the initial DFT (QE/PWscf) calculations were carried out using 80 Ry as energy cut off and 800 Ry as the electron density cutoff. In PWCOND we also used 40 *k*-points in the *y* direction (direction perpendicular to transmission) of the orthogonal unit cell, checking that results were converged up to 110 *k*-points. One can find more information about the *k*-grid convergence in the Supporting Information.

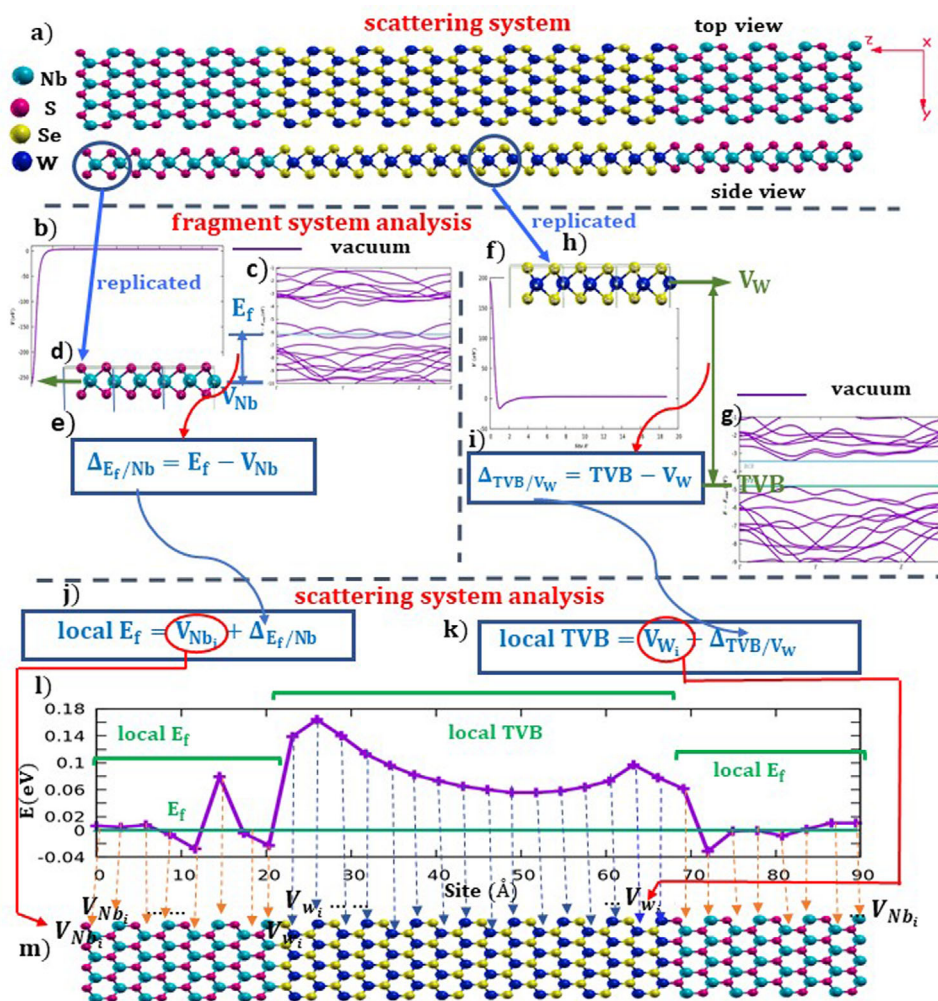


Figure 1. Analysis of the electrostatic potential for the NbS₂/WSe₂ LH. The titles in the figure refers to sections as follows: “scattering system” a); “fragment system analysis” b–i); “scattering system analysis” j–m): a) top and side view of LH with definition of fragments and b–d) NbS₂ fragment: b) electrostatic potential from the Nb nucleus into the vacuum, c) band structure, d) replicated NbS₂ fragment (side view), and e) $\Delta_{E_f/Nb}$ = difference between the on-site potential on the Nb atom and the Fermi energy (E_f) of the NbS₂ fragment; f–i) WSe₂ fragment: f) electrostatic potential from the W nucleus into the vacuum, g) band structure, h) replicated WSe₂ fragment (side view), i) Δ_{TVB/V_W} = difference between the on-site potential on W atom and the top of the valence band (TVB) of the WSe₂ fragment, j) the local Fermi level for the NbS₂ component of the scattering system is obtained by combining the Nb onsite potential in the scattering system (indicated as V_{Nb_i} values) with the $\Delta_{E_f/Nb}$ NbS₂ fragment quantity obtained in (e), and j) the local TVB for the WSe₂ component of the scattering system is obtained by combining the W onsite potential in the scattering system (indicated as V_{W_i} values) with the Δ_{TVB/V_W} WSe₂ fragment quantity obtained in (i); m–l) the atomistic model m) is depicted again and the final band alignment l) is plotted.

2.2. The Analysis Method: Fragment Decomposition and Electrostatic Potential Descriptor

To achieve a deeper understanding of DFT and transport simulations we employ a basic approach for analyzing the electronic band structure of complex systems as proposed in ref. [17], here slightly refined as described hereafter and schematically illustrated in **Figure 1**. This approach relies on two main pillars: 1) decomposing a complex system (here the LH) in terms of individual fragments (here the NbS₂ and WSe₂ extended phases), and thus exploiting the information available on such simpler systems to quantitatively dissect and predictively understand the behavior of the complex system, and 2) using the electro-

static potential as a basic and unifying descriptor of transport phenomena.

In detail, we first conduct DFT band structure simulations on a given LH atomistic model, named the “scattering system,” see **Figure 1a**. We then select two fragments in this scattering system: i) one corresponding to a NbS₂ (orthogonal) unit cell and ii) one corresponding to a WSe₂ (orthogonal) unit cell, and we replicate them according to the precise geometry of the scattering system to produce NbS₂ and WSe₂ extended phases, see **Figure 1d,h**, respectively. Note in passing that the lattice parameter in the y direction resulting from relaxation is a tradeoff between the lattice parameters of NbS₂ and WSe₂ extended phases, and it is important to consider such average geometry in the leads to get

an accurate electrostatic potential analysis, see the discussion below. We recall that NbS₂ is metallic as apparent from its band structure (Figure 1c), while WSe₂ is a semiconductor (see the band structure in Figure 1g). On such pure-phase fragments we calculate the electrostatic potential from Nb and W atoms to the vacuum, see the plots in Figure 1b,f, and draw basic fragment quantities, i.e., i) for NbS₂ the difference between the on-site electrostatic potential on the Nb atom (V_{Nb}) and the Fermi energy (E_f) which we name $\Delta_{E_f/\text{Nb}}$, Figure 1e, ii) for WSe₂ the difference between the on-site electrostatic potential on the W atom (V_{W}) and the TVB which we name $\Delta_{\text{TVB}/V_{\text{W}}}$. For the scattering system, we then calculate the on-site electrostatic potential on the Nb and W atoms, Figure 1m. Finally, we merge the analysis of the electrostatic potential and the band structure of the fragment and composite (scattering) systems by adding the $\Delta_{E_f/\text{Nb}}$ and $\Delta_{\text{TVB}/V_{\text{W}}}$ fragment quantities to the on-site electrostatic potentials of the scattering system to obtain the band alignment, i.e., the local Fermi energy for the metal NbS₂ component, Figure 1j, and the local TVB for the semiconductor WSe₂ component, Figure 1k. The final result is illustrated in the plot of Figure 1l.

In passing, we note that the electrostatic potential is the main component of the Kohn–Sham potential, which provides the self-consistent background on which electrons move. What is lacking in the electrostatic potential with respect to the Kohn–Sham one are exchange–correlation terms. However, since such terms are evaluated via a numerical quadrature in DFT codes, we have found it numerically more robust to employ the bare electrostatic potential in our analysis.^[40] It can be recalled that all such quantities as the electrostatic potential, the Kohn–Sham potential, etc., rigorously correlate via the Hohenberg–Kohn theorem, so that any of them can be used indifferently. Also, the choice of the site where to calculate the electrostatic potentials is in principle irrelevant: in the present work we chose on-site atomic electrostatic potentials (i.e., on the sites of the nuclei) because they are easier to identify precisely from the atomic coordinates. Finally, it can be noted that the fragments must be taken far enough from the interfaces to avoid interface effects on the analysis: to this end we performed convergence tests by increasing the size of the scattering region from a 4 + 4 to an 8 + 8 system (where $N + N$ indicates the number of orthogonal unit cells included) until we got a flat behavior of the on-site potentials in the middle of the NbS₂ metal component. Clearly, the WSe₂ being a semiconductor, the convergence to a flat potential is slower, and a residual minor shift in potential is still present (see Figure S3 in the Supporting Information, for the plot of the potential on W atoms for the 10+10 system). These long-range effects are better and can be properly taken into account via multiscale modeling^[17,41] and we leave them to a future investigation.

3. Results and Discussion

3.1. Structure Generation

To generate an atomistic model of a WSe₂//NbS₂ LH, we first validated the accuracy of our DFT approach in terms of prediction of the geometrical features of WSe₂ and NbS₂ ML phases. The lattice parameters from previous-theory for WSe₂ and NbS₂ ML phases are: 3.319 Å and 3.344 Å, respectively,^[42] very close to our DFT-predicted (full DFT geometry relaxation including

cell axes) are: 3.323 Å and 3.346 Å, respectively. We then built up three systems of increasing size by matching ($N + N$) replicated orthogonal unit cells of WSe₂ and NbS₂, where N is the number of unit cells of each component, and subjected the resulting system to full DFT geometry relaxation (relaxation included cell axes) and band structure and electrostatic potential analysis. We considered 4 + 4, 6 + 6, and 8 + 8 WSe₂//NbS₂ systems, and the 8 + 8 system was selected for transmission analysis because the electrostatic potential profile was tested to be at convergence, as discussed in Figure S2 (Supporting Information). The atomistic model outcome of this step is depicted in Figure S1 (Supporting Information). It should be noted that the mismatch between the hexagonal symmetry of the ML phases and the orthogonal unit cells needed for the successive transport simulations makes that we have two slightly different WSe₂//NbS₂ interfaces on the right- and left-hand sides.

3.2. Electrostatic Potential Analysis

We apply the analysis scheme of Section 2.2 to the 8 + 8 WSe₂//NbS₂ LH system (see Figure 1a). The resulting band alignment, i.e., the local Fermi energy (E_f) for the metal NbS₂ component and the local TVB for the semiconductor WSe₂ component, is reported in Figure 2. In keeping with the fact that NbS₂ is a metal, we find a nearly flat local Fermi energy far from the interfaces in Figure 2, which is consistent with a zero electric field and potential gradient. Also, the local TVB on the W atoms is flat far enough from the interfaces. It can be noted that a flat local E_f in NbS₂ far from the interfaces is needed to choose these sites as leads of the transmission simulations of Section 3.3 and to allow for a precise projection of the wave function of the scattering system onto the wave function of the reference system. It can also be noted the asymmetric profile of the local TVB indicating that there are two slightly different interfaces in the chosen LH, due to geometric nonequivalence reasons.

The two interface dipole moments must however be equal in absolute value and opposite in sign so as to cancel each other, since we are working with plane-wave codes and periodic models (see the discussion in Section S3 of the Supporting Information, for the 4 + 4 WSe₂//NbS₂ LH system; Figures S4 and S5). These effects are anyway minor, and we did not further investigate them. It is instead worthwhile noting that the local Fermi energy in the middle of the unit cell coincides with the system Fermi energy up to a hundredth of an eV proving the accuracy of the chosen analysis strategy. Also, it can be noted that there is a difference between the system work function in the fully relaxed and fragment unit cells of pure NbS₂ amounting to 0.15 eV, while the difference between the local TVB in relaxed and fragment unit cells of pure WSe₂ is 0.11 eV (see the Supporting Information), implying some long-range relaxation effects in a mesoscopic LH (we leave investigation of these long-range effects to a future multiscale investigation^[17,41]). To provide more details, Figure S6 (Supporting Information) compares the DOS of fragments taken from the scattering region with the fully relaxed unit cells of WSe₂ and NbS₂ ML systems.

Finally, as a main outcome of our analysis, we single out the jumps in the local E_f and TVB at the interfaces due to interfacial potential gradients. We quantify these jumps to be of the order of 0.1–0.2 eV, providing an estimate of the Schottky barrier

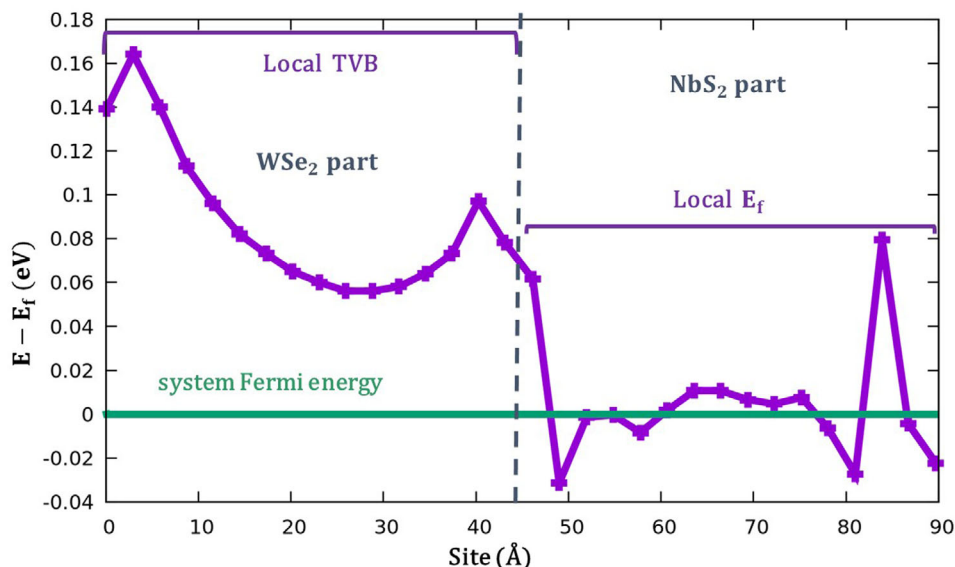


Figure 2. Local TVB on the W atoms and local Fermi energy (E_f) on the Nb atoms of the 8 + 8 $WSe_2//NbS_2$ LH.

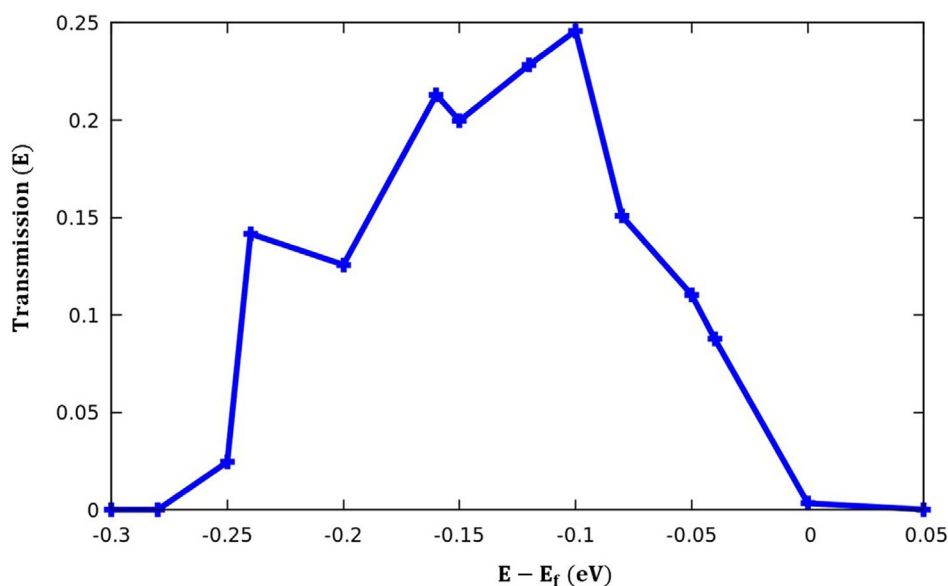


Figure 3. The transmission coefficient as calculated for our $WSe_2//NbS_2$ LH model right below the Fermi energy.

(see below). Note that the Schottky barrier is negative in this system.

3.3. Transmission Simulations

We perform transmission simulations for the scattering system, choosing a NbS_2 orthogonal unit cell far from the interfaces as a left lead, followed by three NbS_2 unit cells, eight WSe_2 unit cells, three other NbS_2 unit cells, and one NbS_2 orthogonal unit cell as the right lead, as shown in Figure 1a. As reference systems, we perform band structure calculations of NbS_2 and WSe_2 fragments using the geometry extracted from the relaxed geometry of the scattering system. We recall

that the cell dimension in the γ direction (perpendicular to the transport direction) does not coincide with the equilibrium one of either NbS_2 or WSe_2 pure ML extended phases, but it is a compromise between the two as obtained from the relaxation of the $WSe_2//NbS_2$ LH, and therefore analogously also the corresponding wave functions. The transport coefficient as evaluated by the PWCOND code from the left lead through the central region of the scattering system to the right lead is shown in **Figure 3**, and has a reasonably smooth profile with a sizeable maximum reading 0.25. The $WSe_2//NbS_2$ LH therefore appears to be a robust and suitable system for use in electronic devices.

For an alternative simplified analysis, we also calculated the effective mass of electron in NbS_2 and WSe_2 pure relaxed unit cells

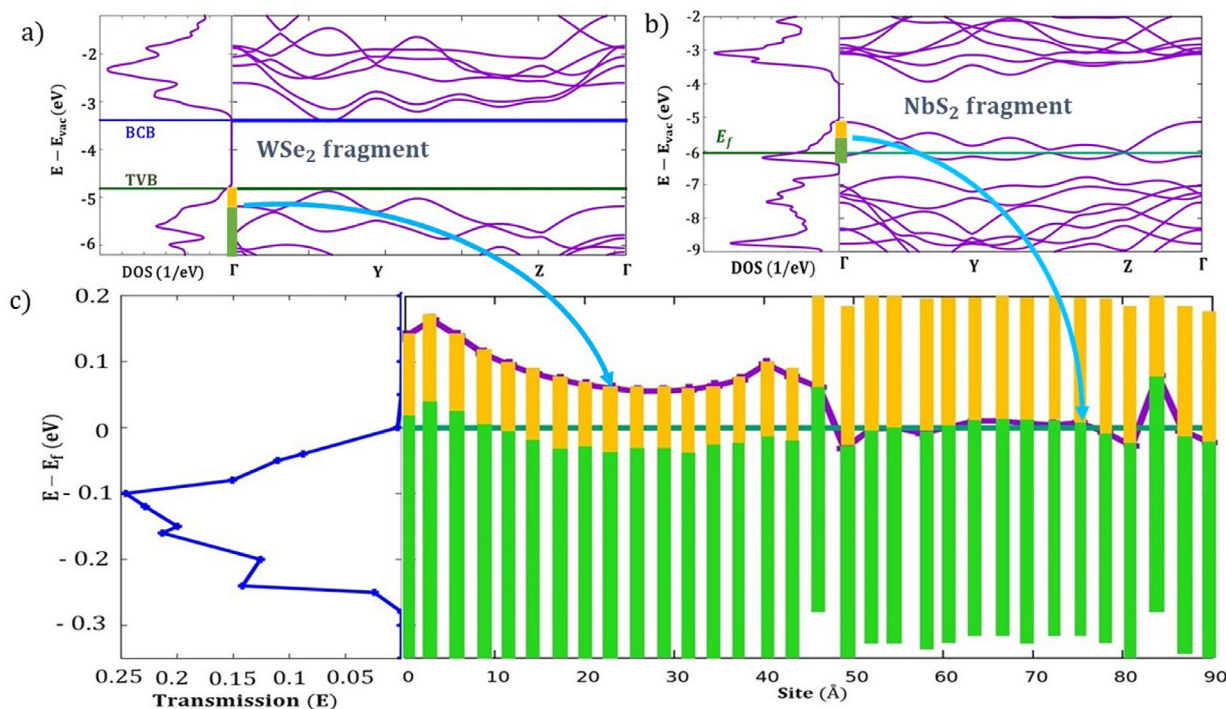


Figure 4. Our approach to find the energy interval of nonzero transmission: a) DOS and band structure of WSe₂ fragment, b) DOS and band structure of NbS₂ fragment, and c) transmission of WSe₂//NbS₂ LH and band alignment procedure to find the states for electron transmission using the color bars from (a) and (b) and placing them accordingly to the local E_f and TVB.

and in the WSe₂//NbS₂ LH, see Section S6 of the Supporting Information. The obtained values show that the electron mobility decreases when the two TMCDs come together to form the LH, which is consistent with a reduced but finite transmission coefficient in Figure 3.

Interestingly, we can use the DOS of the pure phases and the band alignment profile of Figure 2 to deepen our analysis and find the energy intervals (the range of bias) in which we expect finite electron transport and even to obtain a quick estimate of the transmission coefficient in Figure 3, thus checking its consistency and physical interpretation.

By convoluting in fact the band structure of the pure phases and the electrostatic potential profile, we can roughly predict the number of states available for transmission in each NbS₂ or WSe₂ units, thus finding, e.g., where a zero transmission coefficient is to be expected. In **Figure 4**, we divide the ML-phase DOS in a green and a yellow part to distinguish the region of higher density of states (in green) from the region of lower density of states (in yellow). This distinction is of course arbitrary but is useful to stress that the yellow regions are “tails” of the DOS with a significantly lower density of states than the green regions. We then align these “DOS bars” taken from the regular ML phases along the transmission direction by positioning them at each Nb and W atom and shifting them in the energy scale according to the value of the electrostatic potential on the given atom. In this way we can identify values of bias at which we expect that there will or will not be enough states available for transmission on the basis of the values of the DOS. It is worthwhile noting that the limited energy width of the high DOS region in NbS₂ and especially the Nb atoms at the interface mostly affected by the

interface dipole and whose local E_f is therefore shifted to higher energies are the ones responsible for cutting the low-energy end of transmission. Figure 4 pictorially illustrates how our analysis in terms of electrostatic potential, local E_f, etc. turns out to be useful and effective, allowing us to rather precisely single out the range of finite transmission coefficient. We repeat our main conclusion that transmission turns out to be sizeable in an interval of ≈0.28 eV below the Fermi level, reaching a maximum of 0.25.

3.4. Stoichiometry Fluctuations at the LH Interface

Since in the investigated WSe₂//NbS₂ LH two different chalcogenide atoms are present on the two sides of the interface, we considered the possibility that imperfect, stoichiometrically nonsharp interfaces are in fact produced at the experimental level. We explore this possibility differently from the constant stoichiometry simulations of Ref. [33]. Instead, we exchange rows of S atoms with rows of Se atoms or vice versa, and predict the energetics associated with this process and its effect on the on-site electrostatic potentials. In detail, the reaction energy ΔE for a given S ↔ Se replacement is defined as

$$E(\text{perfect system}) + E\left(\frac{1}{2}\text{S}_8\right) \rightarrow E(\text{SF system}) + E\left(\frac{1}{2}\text{Se}_8\right) \quad (1)$$

where “SF system” is the system with stoichiometry fluctuations. An example of such reaction energy is given in Section S7 of the Supporting Information. From the energy point of view, in general we find that the structures in which S atoms replace Se atoms are the most stable ones, i.e., the corresponding transformation energy is negative. To know how the physical properties of the LH

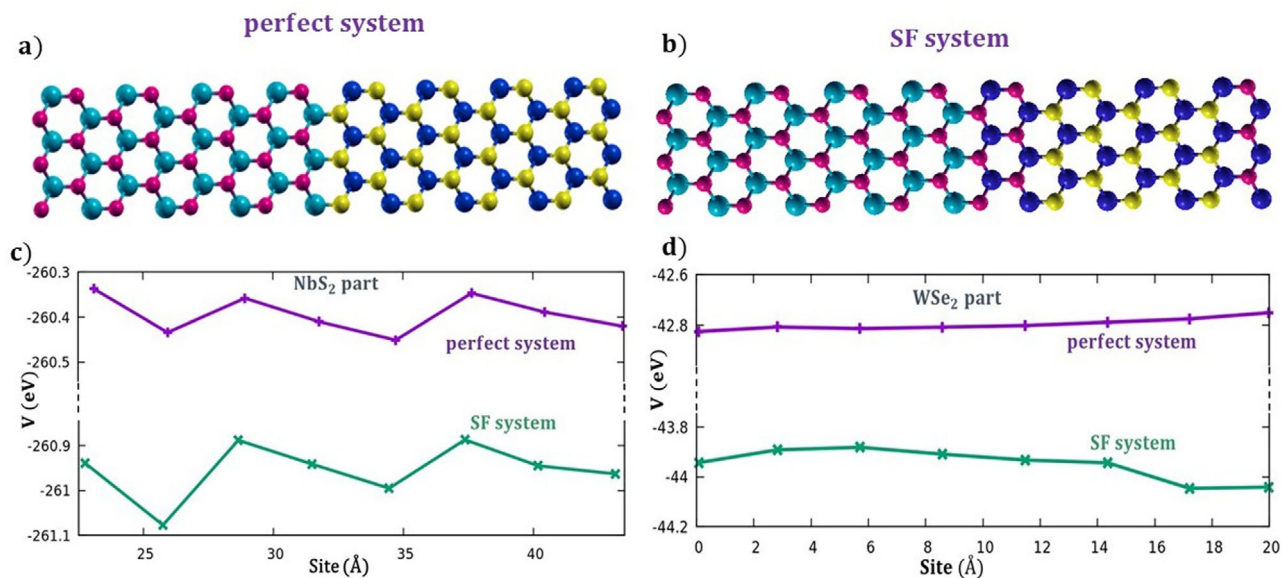


Figure 5. Stoichiometry fluctuation at the interfaces of 4 + 4 WSe₂// NbS₂ LH: a) perfect system structure, b) stoichiometry fluctuated (SF) system, c) comparison between potential on Nb atoms in the perfect and SF systems, and d) comparison between potential on W atoms in the perfect and SF systems.

are affected by these stoichiometry fluctuations, we then studied the electrostatic potential on the Nb and W atoms, using as per our approach the electrostatic potential as a simplified but accurate descriptor of transport phenomena. **Figure 5** compares the electrostatic potential on the Nb and W atoms between systems with and without stoichiometric fluctuations.

The difference between on-site potential of Nb atoms in perfect 4 + 4 WSe₂//NbS₂ LH is in the range 0.031–0.104 eV and for W atoms it is between 0.0057 and 0.024 eV. Also, the difference for Nb atoms of stoichiometry fluctuated (SF) system is 0.018–0.138 eV, while for W atoms it is 0.0054–0.0516 eV. The jump in the electrostatic potential is therefore small: it can change a little the Schottky barrier and the band alignment however without leading to a drastic expected change in transmission. Moreover, the increased thermodynamic stability of the system also likely protects it against formation of other defects, therefore leading to improved transmission properties. Note that there are some experimental indications that this phenomenon can indeed occur. For example, it has been found that experimentally that WSe₂ and MoSe₂ can be easily sulfurized during growth of their corresponding sulfur analogs, observed for WSe₂//WS₂^[21] and MoSe₂ leading to formation MoS_xSe_y alloys.^[43] In this sense, our study is in line and can be useful for experimentalists to orient their growth protocols.

4. Conclusions

2D^[1] LH joining two different transition metal dichalcogenides (TMDCs) materials stand out as promising modular unit blocks in future optoelectronic devices^[11] due to their peculiar charge transport and optical response properties.^[2,3] Several examples of such composite interfaces are currently being produced^[7–10] and investigated at both experimental^[20–22] and theoretical^[27–33] levels, with the goal of realizing the ultimate thickness limit for metal/semiconductor in-plane junctions.

At this nanometer scale, first-principles QM simulations are required to predictively model these systems and their behavior with an accuracy comparable with experiment,^[18] and are especially useful when analyzed to interpret in depth computational and experimental^[19] results, and extract basic information on relationships between structure and transport properties.^[16,17]

Here, we use QM modeling to investigate the electronic structure and transport features of a ML-thick NbS₂//WSe₂ LH, as a paradigmatic example of metal/semiconductor 2D hybrid interfaces based on TMDC. We construct and validate convergence of atomistic periodic models of the LH, derive their band structure also exploring sulfur/selenium stoichiometric fluctuations at the interface, and predict electron transport response. An accompanying fragment and electrostatic-potential (plus band alignment) analysis illuminates our findings, and allows us to interpret them in terms of a simple but quantitative model of the junction. We find that the NbS₂//WSe₂ LH is a promising robust in-plane 2D modular junction, with stoichiometric fluctuations possibly stabilizing the system without deteriorating its electronic features, and thus appears suitable to be potentially exploited in an integrated circuit technology going beyond present silicon-based miniaturization level.^[12]

Supporting Information

Supporting Information is available from the Wiley Online Library or from the author.

Acknowledgements

The authors acknowledge financial support from the QUEFORMAL FET-Open EU project (Grant Agreement 829035) and from the MIUR PRIN Five2D project (2017SRJEJH), and computational support from the Cineca Supercomputing Center for the LH-FET grant. The authors are also grateful to Alexander Smogunov for useful discussions and hints about

transmission simulations and to Enrique González Marín for providing useful scripting.

Conflict of Interest

The authors declare no conflict of interest.

Keywords

background electrostatic potential, electron transport, fragment decomposition, optoelectronic devices, quantum mechanical modeling, stoichiometric fluctuations

Received: July 23, 2020

Revised: October 3, 2020

Published online: October 27, 2020

- [1] K. S. Novoselov, D. Jiang, F. Schedin, T. J. Booth, V. V. Khotkevich, S. V. Morozov, A. K. Geim, *Proc. Natl. Acad. Sci. USA* **2005**, *102*, 10451.
- [2] B. Radisavljevic, A. Kis, *Nat. Mater.* **2013**, *12*, 815.
- [3] K. K. Liu, W. Zhang, Y.-H. Lee, Y.-C. Lin, M.-T. Chang, C.-Y. Su, C.-S. Chang, H. Li, Y. Shi, H. Zhang, C.-S. Lai, L.-J. Li, *Nano Lett.* **2012**, *12*, 1538.
- [4] J. D. Cain, F. Shi, J. Wu, V. P. Dravid, *ACS Nano* **2016**, *10*, 5440.
- [5] Y. Gong, S. Lei, G. Ye, B. Li, Y. He, K. Keyshar, X. Zhang, Q. Wang, J. Lou, Z. Liu, R. Vajtai, W. Zhou, P. M. Ajayan, *Nano Lett.* **2015**, *15*, 6135.
- [6] N. Choudhary, J. Park, J. Y. Hwang, H.-S. Chung, K. H. Dumas, S. I. Khondaker, W. Choi, Y. Jung, *Sci. Rep.* **2016**, *6*, 25456.
- [7] C. Huang, S. Wu, A. M. Sanchez, J. J. P. Peters, R. Beanland, J. S. Ross, P. Rivera, W. Yao, D. H. Cobden, X. Xu, *Nat. Mater.* **2014**, *13*, 1096.
- [8] X. Duan, C. Wang, J. C. Shaw, R. Cheng, Y. Chen, H. Li, X. Wu, Y. Tang, Q. Zhang, A. Pan, J. Jiang, R. Yu, Y. Huang, X. Duan, *Nat. Nanotechnol.* **2014**, *9*, 1024.
- [9] Y. Gong, J. Lin, X. Wang, G. Shi, S. Lei, Z. Lin, X. Zou, G. Ye, R. Vajtai, B. I. Yakobson, H. Terrones, M. Terrones, B. K. Tay, J. Lou, S. T. Pantelides, Z. Liu, W. Zhou, P. M. Ajayan, *Nat. Mater.* **2014**, *13*, 1135.
- [10] X. Hong, J. Kim, S.-F. Shi, Y. Zhang, C. Jin, Y. Sun, S. Tongay, J. Wu, Y. Zhang, F. Wang, *Nat. Nanotechnol.* **2014**, *9*, 682.
- [11] D. Marian, E. Dib, T. Cusati, E. G. Marin, A. Fortunelli, G. Iannaccone, G. Fiori, *Phys. Rev. Appl.* **2017**, *8*, 054047.
- [12] G. Iannaccone, F. Bonaccorso, L. Colombo, G. Fiori, *Nat. Nanotechnol.* **2018**, *13*, 183.
- [13] Materials Design: <https://www.materialsdesign.com/medea-software> (accessed: October 2020).
- [14] European Materials Research Society (E-MRS): <https://www.european-mrs.com/quantum-wise> (accessed: October 2020).
- [15] NanoCAD ViDES: <http://vides.nanotcad.com/vides/> (accessed: October 2020).
- [16] L. Jelver, D. Stradi, K. Stokbro, K. W. Jacobsen, **2019**, arXiv:1911.09521.
- [17] T. Cusati, G. Fiori, A. Gahoi, V. Passi, M. C. Lemme, A. Fortunelli, G. Iannaccone, *Sci. Rep.* **2017**, *7*, 5109.
- [18] W. Jang, K. Kang, A. Soon, *Nanoscale* **2015**, *7*, 19073.
- [19] M. Kruskopf, R. E. Elmquist, *Metrologia* **2018**, *55*, R27.
- [20] C. Zhang, Y. Chen, J. K. Huang, X. Wu, L. J. Li, W. Yao, J. Tersoff, C. K. Shih, *Nat. Commun.* **2016**, *7*, 1.
- [21] H. Li, P. Li, J. K. Huang, M. Y. Li, C. W. Yang, Y. Shi, X. X. Zhang, L. J. Li, *ACS Nano* **2016**, *10*, 10516.
- [22] H. G. Shin, H. S. Yoon, J. S. Kim, M. Kim, J. Y. Lim, S. Yu, J. H. Park, Y. Yi, T. Kim, S. C. Jun, S. Im, *Nano Lett.* **2018**, *18*, 1937.
- [23] Y. Katagiri, T. Nakamura, A. Ishii, C. Ohata, M. Hasegawa, S. Katsumoto, T. Cusati, A. Fortunelli, G. Iannaccone, G. Fiori, S. Roche, *Nano Lett.* **2016**, *16*, 3788.
- [24] S. Liu, J. Li, B. Shi, X. Zhang, Y. Pan, M. Ye, R. Quhe, Y. Wang, H. Zhang, J. Yan, L. Xu, *J. Mater. Chem. C* **2018**, *6*, 5651.
- [25] X. Zhang, Z. Jin, L. Wang, J. A. Hachtel, E. Villarreal, Z. Wang, T. Ha, Y. Nakanishi, C. S. Tiwary, J. Lai, L. Dong, J. Yang, R. Vajtai, E. Ringe, J. C. Idrobo, B. I. Yakobson, J. Lou, V. Gambin, R. Koltun, P. M. Ajayan, *ACS Appl. Mater. Interfaces* **2019**, *11*, 12777.
- [26] H. Mine, A. Kobayashi, T. Nakamura, T. Inoue, S. Pakdel, D. Marian, E. Gonzalez-Marín, S. Maruyama, S. Katsumoto, A. Fortunelli, J. J. Palacios, *Phys. Rev. Lett.* **2019**, *123*, 146803.
- [27] C. Mu, W. Wei, J. Li, B. Huang, Y. Dai, *Mater. Res. Express* **2018**, *5*, 046307.
- [28] Y. An, M. Zhang, D. Wu, Z. Fu, K. Wang, *J. Mater. Chem. C* **2016**, *4*, 10962.
- [29] Y. N. Wen, M. G. Xia, S. L. Zhang, *Appl. Surf. Sci.* **2016**, *371*, 376.
- [30] W. Wei, Y. Dai, B. Huang, *Phys. Chem. Chem. Phys.* **2016**, *18*, 15632.
- [31] X. Ding, S. Zhang, M. Zhao, Y. Xiang, K. H. Zhang, X. Zu, S. Li, L. Qiao, *Phys. Rev. Appl.* **2019**, *12*, 064061.
- [32] H. Zhu, C. Zhou, Y. Wu, W. Lin, W. Yang, Z. Cheng, X. Cai, *Surf. Sci.* **2017**, *661*, 1.
- [33] Z. Cao, M. Harb, S. Lardhi, L. Cavallo, *J. Phys. Chem. Lett.* **2017**, *8*, 1664.
- [34] P. Giannozzi, S. Baroni, N. Bonini, M. Calandra, R. Car, C. Cavazzoni, D. Ceresoli, G. L. Chiarotti, M. Cococcioni, I. Dabo, A. D. Corso, S. de Gironcoli, S. Fabris, G. Fratesi, R. Gebauer, U. Gerstmann, C. Gougoussis, A. Kokalj, M. Lazzeri, L. Martin-Samos, N. Marzari, F. Mauri, R. Mazzarello, S. Paolini, A. Pasquarello, L. Paulatto, C. Sbraccia, S. Scandolo, G. Sclauzero, A. P. Seitsonen, A. Smogunov, P. Umari, R. M. Wentzcovitch, *J. Phys.: Condens. Matter* **2009**, *21*, 395502.
- [35] P. Giannozzi, O. Andreussi, T. Brumme, O. Bunau, M. B. Nardelli, M. Calandra, R. Car, C. Cavazzoni, D. Ceresoli, M. Cococcioni, N. Colonna, I. Carnimeo, A. Dal Corso, S. de Gironcoli, P. Delugas, R. A. DiStasio, A. Ferretti, A. Floris, G. Fratesi, G. Fugallo, R. Gebauer, U. Gerstmann, F. Giustino, T. Gorni, J. Jia, M. Kawamura, H.-Y. Ko, A. Kokalj, E. Küçükbenli, M. Lazzeri, M. Marsili, N. Marzari, F. Mauri, N. L. Nguyen, H.-V. Nguyen, A. Otero-de-la-Roza, L. Paulatto, S. Poncé, D. Rocca, R. Sabatini, B. Santra, M. Schlipf, A. P. Seitsonen, A. Smogunov, I. Timrov, T. Thonhauser, P. Umari, N. Vast, X. Wu, S. Baroni, *J. Phys.: Condens. Matter* **2017**, *29*, 465901.
- [36] J. Perdew, K. Burke, M. Ernzerhof, *Phys. Rev. Lett.* **1996**, *77*, 3865.
- [37] S. Grimme, *J. Comput. Chem.* **2004**, *25*, 1463.
- [38] H. J. Choi, J. Ihm, *Phys. Rev. B* **1999**, *59*, 2267.
- [39] A. Smogunov, A. Dal Corso, E. Tosatti, *Phys. Rev. B* **2004**, *70*, 045417.
- [40] This is especially true for the W atom, whose pseudopotential may contain f orbitals, which also complicate its use in the PWCOND routine.
- [41] V. Passi, A. Gahoi, E. G. Marin, T. Cusati, A. Fortunelli, G. Iannaccone, G. Fiori, M. C. Lemme, *Adv. Mater. Interfaces* **2019**, *6*, 1801285.
- [42] Computational 2D materials database, <https://cmrdb.fysik.dtu.dk/c2db/>
- [43] S. H. Su, W.-T. Hsu, C.-L. Hsu, C.-H. Chen, M.-H. Chiu, Y.-C. Lin, W.-H. Chang, K. Suenaga, J.-H. He, L.-J. Li, *Front. Energy Res.* **2014**, *2*, 27.